

**Microstructural Mitigation of Hydrogen Environment  
Embrittlement of Ultra-high Strength AerMet™ 100**

*Yongwon Lee and Richard P. Gangloff*

**DISTRIBUTION STATEMENT A**  
Approved for Public Release  
Distribution Unlimited

**20060713054**

## Mitigation of Hydrogen Environment Embrittlement in AerMet™ 100 by Microstructural Modification

Yongwon Lee and Richard P. Gangloff

**DISTRIBUTION STATEMENT A**  
Approved for Public Release  
Distribution Unlimited

### ABSTRACT

AerMet™ 100, a secondary precipitation hardened martensitic steel, has excellent strength ( $\sigma_{YS} = 1725$  MPa) and toughness ( $K_{IC} = 130$  MP $\sqrt{\text{cm}}$ ) when optimally tempered at 482°C. However, it is susceptible to severe hydrogen environment assisted cracking (HEAC) in near-neutral 3.5% NaCl at very low threshold stress intensities ( $K_{TH}$ ) and with rapid Stage II plateau rates for subcritical crack propagation ( $da/dt_{II}$ ). Interaction between environmental hydrogen and the complex microstructure influences the HEAC response, and modifications to heat treatment could improve HEAC resistance, particularly considering H-trap interactions. The effect of aging condition on HEAC of AerMet™ 100 was examined. Specimens were aged for 5 h at 482°C, 510°C and 538°C or studied in the as-quenched condition; then stressed at slow constant displacement rate in 3.5% NaCl at two polarization levels. When polarized to  $-0.9 V_{SCE}$ , all aged specimens showed substantial HEAC with low  $K_{TH}$  (10~20% of  $K_{IC}$ ) and high  $da/dt_{II}$  (up to 30nm/s); but the as-quenched condition had substantially higher  $K_{TH}$  (70% of  $K_{IC}$ ) and slow  $da/dt_{II}$  (1 nm/s). The HEAC path was mostly transgranular for all conditions, but predominantly intergranular when aged at 538°C. The aging independence of HEAC at  $-0.9 V_{SCE}$  may be consistent with a mechanistic explanation based on H diffusion control of crack growth rate, but material dependent terms in the model for  $da/dt_{II}$  and the detail of the model are uncertain. It is not possible to design alloy composition and processing conditions based on such existing models. Qualitatively, increasing incoherence of  $M_2C$  precipitates does not result in reduced  $da/dt_{II}$ , perhaps due to the counterbalancing effects of increased trapping causing reduced H diffusivity but increased H solubility. Relatively low H-trap binding energy of these precipitates for all tempers examined prevents beneficial shielding of H partition to martensite lath/packet boundary interfaces where such segregation enables decohesion. The absence of uniformly distributed carbide H traps in the non-aged condition increases the HEAC crack growth rate, following this analysis, but lack of thin-film austenite may reduce martensite boundary cracking compared to that provided by aging at 482°C and 510°C. The presence of greatly increased intra-lath austenite appears to protect the martensite boundary to allow IG HEAC for the 538°C temper. These experiments build on IHAC and HEAC results for peak strength/toughness AerMet™ 100 and provide further understanding of the role of microstructure in HEAC necessary to predict and optimize the HEAC resistance of modern UHSS. However, this work does not provide strong improvement in cracking resistance, demonstrating the overriding importance of HEAC to this class of steels and the challenge in microstructural design.

## I. Introduction

When aged at 482°C to achieve peak toughness, AerMet™ 100 is susceptible to internal hydrogen assisted cracking (IHAC)<sup>[1]</sup>, as well as hydrogen environment assisted cracking (HEAC) in near-neutral 3.5% NaCl<sup>[2]</sup> at very low threshold stress intensities ( $K_{TH}$ ) and rapid Stage II plateau rates for subcritical crack propagation ( $da/dt_{II}$ ) comparable to older UHSS<sup>[3]</sup>. Contrary to the IG HEAC fracture path of older UHSS, hydrogen assisted cracking is predominantly transgranular in AerMet™ 100. This change is attributed to improved austenite boundary purity, and significant H trapping that promotes decohesion of martensite lath and packet interfaces<sup>[1,4,5]</sup>. Accordingly, it is hypothesized that changes in microstructure caused by varying heat treatments may alter the fracture path of HEAC. The kinetics of HEAC in ultra-high strength alloys are likely governed by atomic hydrogen (H) diffusion from the reacting crack tip surface to damage sites located within the fracture process zone (FPZ), of order 1  $\mu\text{m}$  from the surface<sup>[3]</sup>. Accordingly, the trap-sensitive diffusivity of H ( $D_H$ ) and local reversibly-trapped H concentration ( $C_H$ ) are critical factors that influence threshold and crack growth rate properties. Each of these parameters is sensitive to microstructure, as understood by the binding energy ( $E_B$ ) between H and the trap site<sup>[5]</sup>. Although the microstructural evolution of AerMet™ 100 for various heat treatments is well documented<sup>[6-10]</sup>, precise consequences for HEAC have not been studied. Modifications to microstructure can be critical in HEAC mitigation, and the results from this research provide an initial basis to reduce cracking susceptibility.

### I.A. Hydrogen Trapping and Microstructure in AerMet™ 100

Hydrogen is trapped at multiple microstructural features in AerMet™ 100, including nanoscale carbides ( $M_2C = (Cr,Mo)_2C$ ), cementite, undissolved alloy carbides, martensite laths and packet interfaces, prior austenite grain boundaries, and dislocations<sup>[4-9]</sup>. These traps play a dominant role in hydrogen assisted cracking (HAC) due to strong influences on the local solubility ( $C_H$ ) and diffusivity ( $D_H$ ) of hydrogen; and the exact properties of each trap is determined by the heat treatment once the bulk composition is fixed. According to previous studies of AerMet™ 100<sup>[1,2,4,5]</sup>, the most critical H traps relevant to IHAC and HEAC in the peak toughness temper (482°C) are those associated with  $M_2C$  carbides and martensite lath and packet boundaries. Those studies concluded that nano-scale, coherent and homogeneously dispersed  $M_2C$  carbide traps have low H-trap binding energies ( $E_B \sim 11$  kJ/mol) and are reversible upon

stress application, while martensite boundaries have higher binding energies ( $E_B \sim 61$  kJ/mol) and are more akin to irreversible traps. In IHAC of AerMet™ 100, crack tip stress causes H repartitioning from precharged  $M_2C$  carbide traps to interconnected martensite interfaces within the fracture process zone (FPZ) to cause severe TG cracking<sup>[1,4,5]</sup>. In HEAC, H diffuses to the same martensite interfaces and causes similar TG fracture<sup>[2]</sup>. It was speculated that uniformly distributed  $M_2C$  carbide traps may beneficially impede H accumulation at (or diffusion to) the higher energy martensite traps, but this effect was not evident in the peak-toughness condition<sup>[2]</sup>.

When aged at higher temperatures or extended duration, the  $M_2C$  carbides increase in size and lose coherency with the matrix<sup>[6,9]</sup>, likely increasing H-trap binding energy<sup>[5]</sup>. As long as particle coarsening does not change distribution uniformity, such an increase in  $E_B$  may allow the carbides to act as H diffusion barriers and also trap H away from susceptible boundaries and increase resistance to HEAC. This effect will be better achieved through higher temperature tempering rather than extended duration aging because studies suggest that extended isothermal aging causes sudden deterioration in the yield strength and alters  $M_2C$  distribution in a manner less predictable than those caused by temperature adjustment<sup>[7,8]</sup>. Therefore, aging time was fixed at 5 h, and aging temperature was varied. The exact value of  $E_B$  for each trap site in each tempering condition has not been investigated. Such detailed work is only justified if initial characterization suggests substantially improved resistance to HEAC.

### I.B. Microstructure Design

Four conditions were chosen to control the critical microstructural features in AerMet™ 100, selected based on detailed existing studies of microstructure<sup>[6-9]</sup>. These heat treatments retain the high strength ( $\sigma_{YS} > 1300$  MPa) and toughness ( $K_{IC} > 100$  MPa $\sqrt{m}$ ) of this alloy steel. At the aging temperature of 482°C, the predominant rod-shaped  $M_2C$  carbides are approximately 9 nm long and 3 nm in diameter and uniformly distributed in the matrix. These carbides are coherent with the matrix and coexist with solute zones at this temperature<sup>[6-9]</sup>. A small amount of thin-film reverted austenite ( $\gamma'$ ) forms between the martensite plates, 0.5%<sup>[6]</sup> or 4%<sup>[9,10]</sup> in volume fraction based on measurements reported by two separate groups.

At 510°C, the volume fraction of  $\gamma'$  increases to 1%<sup>[6]</sup> or 7%<sup>[9,10]</sup> and remains in the thin film inter-plate morphology. The  $M_2C$  carbides increase in size to  $\sim 17$  nm x 6 nm, and begin to lose coherency by both reported accounts<sup>[6,9]</sup>. The Cr content of the carbide reduces slightly to 70%, while the Fe and Mo concentrations increase. At 538°C, the volume fraction of  $\gamma'$

increases to 5.5%<sup>[6]</sup> or perhaps higher<sup>[9,10]</sup> and begins forming intra-plate. The  $M_2C$  carbides increase in size to approximately 28 nm x 10 nm, and further lose coherency with the matrix<sup>[6]</sup>. The Cr content of the carbide further reduces to 65%. In the quenched and cryogenically stabilized condition that precedes aging, the matrix is predominantly unrecovered martensite with 0<sup>[6]</sup> to 3<sup>[10]</sup> vol.% of retained austenite.  $M_2C$  carbides have not formed and there are only undissolved 100-500 nm scale  $MC/M_{23}C_6$  carbides<sup>[6]</sup>. This condition provides the reference for studying the effect of  $M_2C$  and thin-film reverted austenite, due to their absence. Moreover, the martensite is unrecovered and the undissolved carbides do not coarsen during the ages employed. Although large, incoherent carbides are irreversible traps which are reported to dominate HAC in certain steels<sup>[11,12]</sup>, the importance of such particles is challenged and are viewed by the present authors to be unimportant to IHAC and HEAC<sup>[2,3]</sup>. Cementite is absent from AerMet<sup>TM</sup> 100 in both the as-quenched condition and at aging temperatures above 482°C.

#### **I.C. Effect of Applied Electrode Potential on HEAC of AerMet<sup>TM</sup> 100**

The effect of applied electrode potential,  $E_{App}$ , on HEAC of AerMet<sup>TM</sup> 100 was accurately established by various loading methods including slow strain rate<sup>[2]</sup> and step rising load<sup>[13-15]</sup>. Although there is variability in the exact values of  $K_{TH}$ , it is clear that optimal resistance to HEAC in near-neutral 3.5% NaCl exists near -0.6 with respect to the saturated calomel reference ( $V_{SCE}$ ), and severe HEAC occurs at both anodic (-0.5  $V_{SCE}$ ) and cathodic (-0.9  $V_{SCE}$ ) potentials. Two potentials were chosen to probe the interaction of microstructure and electrochemical approaches to mitigate HEAC. The effect of aging on HEAC of AerMet<sup>TM</sup> 100 is isolated by experiments at a single  $E_{App}$  of -0.9  $V_{SCE}$  where cracking is severe for the high strength-toughness microstructure. These experiments are augmented by testing at -0.625  $V_{SCE}$  to establish the effect of aging for the applied potential regime where HEAC in the susceptible peak aged microstructure is substantially mitigated by reduced electrochemical production of H.

#### **I.D. Objectives**

The objective of this research is to quantify the effect of aging condition on the susceptibility of AerMet<sup>TM</sup> 100 to HEAC. Four aging conditions that give good strength and fracture toughness are examined. The  $K_{TH}$  for the onset of HEAC under rising stress intensity and  $da/dt_H$  are determined at two constant electrochemical conditions representing the extremes of crack tip H production and uptake. The HEAC path and morphology are examined compared

to the microstructure produced by different tempering temperatures. These experiments build on IHAC and HEAC results for peak strength/toughness AerMet™ 100 and provide further understanding of the role of microstructure in HEAC necessary to predict and optimize the HEAC resistance of modern UHSS.

## II. Procedure

### II.A. Material and Specimen Design

Specimen design was identical to that used in the peak-age HEAC study<sup>[2]</sup>, as outlined in the previous chapter of this report, with the following exceptions. Eight discs of forged bar of AerMet™ 100, each 15 cm in diameter and 1.6 cm thick, were austenitized at 885°C for 1 h, quenched in liquid nitrogen and cold stabilized for 5 h. Six discs were tempered in vacuum for 5 h and air cooled to obtain two discs per aging temperature: 482°C, 510°C, 538°C. The remaining two pieces were not aged and studied in the as-quenched (AQ) condition. Steel composition was identical to that examined in the HEAC study of peak aged AerMet™ 100<sup>[2]</sup>. The heat treatments and key mechanical properties reported by previous investigators<sup>[6-9]</sup> are summarized in Tables 1 and 2.

HRC	$\sigma_{YS}$ (MPa)	$\sigma_{UTS}$ (MPa)	Reduction in Area (pct)	E (GPa)	$\sigma_o$ (MPa)	$K_{IC}$ (MPa $\sqrt{m}$ )
54	1725	1965	65	194.4	1985	130

Age	HRC	$\sigma_{YS}$ (MPa)	$K_{IC}$ (MPa $\sqrt{m}$ )	Carbide morphology	$\gamma'$ volume fraction (%)
As Quenched	52	1350	123	Undissolved MC/M <sub>23</sub> C <sub>6</sub> carbides	-
482°C 5 h	56	1725	130	Solute zones and coherent M <sub>2</sub> C <sup>[6]</sup> 9 x 3 nm <sup>[6]</sup>	Plate boundary 0.5 <sup>[6]</sup> , 4 <sup>[9]</sup>
510°C 5 h	52	1580	130	Coherent M <sub>2</sub> C <sup>[6,9]</sup> 17 x 6 nm <sup>[6]</sup>	Plate boundary 1 <sup>[6]</sup> , 7 <sup>[9]</sup>
538°C 5 h	48	1380	118	Incoherent M <sub>2</sub> C <sup>[6,9]</sup> 27 x 10 nm <sup>[6]</sup>	Intra-plate 5.5 <sup>[6]</sup>

Single edge micronotch tensile (SENT) specimens were machined with identical methods and dimensions as previously used<sup>[2]</sup>. The Mode I load was applied in the circumferential (C) direction and crack growth occurred in the length (L) direction in the original round-forged bar. To obtain a sharp precrack, a wired SENT specimen was fatigue precracked to a total notch plus crack depth ( $a_0$ ) of 200-2500  $\mu\text{m}$  in moist air at 20 Hz with decreasing maximum stress intensity from 15  $\text{MPa}\sqrt{\text{m}}$  to 5  $\text{MPa}\sqrt{\text{m}}$  and constant stress ratio of 0.10. The longer precracks were required to retain small scale yielding for the stress intensity ( $K$ ) levels of interest in the somewhat lower strength microstructures. Due to the differences in  $a_0$ , some variances were introduced into the loading rate. These experimental variables and possible complicating effects are discussed later.

## II.B. Experimental Setup

The HEAC test setup was identical to previous experiments<sup>[2]</sup> with the following exceptions. The SENT specimen was immersed fully in 3.5% NaCl solution and configured as the working electrode grounded through a wire connected from the specimen to building ground. The potentiostat was operated in floating mode to avoid a ground loop. Experiments were conducted in potentiostatic control with two applied-constant potentials,  $E_{\text{App}}$  of -0.900 or -0.625  $V_{\text{SCE}}$ . All specimens were preloaded quickly to 3  $\text{MPa}\sqrt{\text{m}}$ , within 1 h of specimen polarization, then loaded at a slower-constant rate of grip displacement. The direct current electrical potential difference (dcPD) method was used to measure crack length *in-situ*<sup>[16-18]</sup> in identical fashion to the previous HEAC experiments<sup>[2]</sup>. The applied stress intensity,  $K$ , and threshold stress intensity,  $K_{\text{TH}}$ , were defined as in the previous report<sup>[2]</sup>.  $K_{\text{TH}}^*$  was defined as the  $K$  required to exceed crack growth rate of 1 nm/s. Fracture surfaces were cleaned ultrasonically in acetone then methanol for 10 minutes, dried, and stored in a desiccator. When necessary, specimens were polarized to -1.5  $V_{\text{SCE}}$  in 0.5 M  $\text{H}_2\text{SO}_4$  for 60 s or soaked in 10% HCl for 30 s to remove corrosion products. Scanning electron microscope (SEM) fractographs were obtained using identical conditions as before<sup>[2]</sup>, and the crack advanced from bottom to top of an SEM image.

### III. Results

#### III.A. $K_{TH}$ and Crack Growth Kinetics at $E_{App} = -0.900 V_{SCE}$

When aged at the selected temperatures between 482°C and 538 °C, AerMet™ 100 was susceptible to severe HEAC in neutral 3.5% NaCl for constant applied potential of -0.900  $V_{SCE}$ . Figure 1 shows measured and operationally defined  $K_{TH}$  as a function of aging temperature, with the reference  $K_{IC}$  from Table 2 plotted for each condition. These data show that aging at 482°C and 510°C produced similar HEAC susceptibility at  $K_{TH}$  of 13  $MPa\sqrt{m}$  (11% of  $K_{IC}$  from Table 2) and 13.5  $MPa\sqrt{m}$  (12% of  $K_{IC}$ ), respectively. Tempering at higher temperature (538°C) improved  $K_{TH}$  to 23  $MPa\sqrt{m}$ , 20% of the  $K_{IC}$  for this condition. Remarkably, substantial recovery of cracking resistance was observed for the AQ condition with  $K_{TH}$  of 87  $MPa\sqrt{m}$  (71% of  $K_{IC}$ ). The initial crack length of the AQ specimen was substantially longer (2.5 mm) than other specimens (0.25 ~ 0.76 mm). The  $K_{TH}^*$  followed the same general trend, and the values are listed in Table 3. This form of threshold represents the stress intensity level required to produce a crack growth rate of 1 nm/s, as justified in the preceding chapter of this final report<sup>[2]</sup>.

**Table 3. Summary of HEAC results for  $E_{App} = -0.900 V_{SCE}$**

Heat Treatment	$a_0$ (mm)	Initial $dK/dt$ ( $MPa\sqrt{m}/h$ )	$K_{TH}$ ( $MPa\sqrt{m}$ ) [Figure 1]	$K_{TH}^*$ ( $MPa\sqrt{m}$ )	$da/dt_{II}$ (nm/s) [Figure 2]	Fracture Mode [Figures 3-4]
AQ	2.8	$1.7 \times 10^{-3}$	87	77	1	TG + Branching
482°C	0.24	$6.1 \times 10^{-4}$	13	10.7	10	TG + Branching
510°C	0.30	$5.6 \times 10^{-4}$	13.5	11.6	10	TG + Branching
538°C	0.79	$1.7 \times 10^{-3}$	23	21.7	10	IG

Measured subcritical crack growth kinetics for the various aged microstructures of AerMet™ 100 are similar to previous HEAC experiments<sup>[2]</sup> and reported in Figure 2. Due to the differences in initial crack length, the constant loading rate ( $dK/dt$ ) prior to the onset of subcritical crack growth varied as noted in Figure 2 and Table 2. The Stage I and II regimes of growth behavior are not distinguishable for all specimens in Figure 2, so closer examination is required. For the AQ condition, what appears to be Stage-I growth at high  $K$  is actually H-induced crack branching and tearing at  $K$  below the H-free  $K_{IC}$ , also called Stage-III growth.

Therefore, the flat region below  $K$  of 70 MPa $\sqrt{\text{m}}$  represents Stage-II growth at  $da/dt_{II}$  far below that of the other aging temperatures at the same electrochemical condition, and Stage-I growth is not shown in Figure 2 for this specimen. For this AQ condition, load and dcPD data were not collected for stress intensity levels below  $K$  of 30 MPa $\sqrt{\text{m}}$ . Clearly subcritical HEAC occurred, but the two measures of threshold are uncertain due to this loss of data. The value of  $K_{TH}$  (87 MPa $\sqrt{\text{m}}$ ) plotted in Figure 1 for the AQ condition is particularly suspect. This interpretation is confirmed by fractographic observations presented in Section III.B. The specimen aged at 538°C displays somewhat erratic behavior and limited data collection, which was due to a machine malfunction that caused premature truncation of the data at  $K \sim 30$  MPa $\sqrt{\text{m}}$ . Nonetheless, the sharply increasing  $da/dt$  around  $K$  of 20 MPa $\sqrt{\text{m}}$  for this aging temperature correctly represents Stage-I HEAC growth. The crack kinetics response for the 510°C age is nearly identical to that of the peak-aged condition with the Stage-II behavior somewhat dependent on  $K$ . The  $da/dt$  values for the 538°C age show modestly delayed Stage-I to Stage-II transition at a higher  $K$  level. The Stage-II crack growth rate,  $da/dt_{II}$ , was approximately the same at 10nm/s for the 482°C, 510°C and 538°C tempers. However,  $da/dt_{II}$  for the AQ condition was significantly slower at 1 nm/s, a result not compromised by the missing data for the lower  $K$  regime.

### III.B. Effect of Aging Temperature on HEAC Morphology at $E_{App} = -0.900 V_{SCE}$

Fractographic analyses show that HEAC occurred at  $E_{App} -0.9 V_{SCE}$  for all aging conditions of AerMet™ 100, but such subcritical cracking was limited to a very small region (< 100  $\mu\text{m}$ ) for the AQ condition. The results of this SEM analysis are shown in Figure 3. For the AQ condition, the entire loading range from 5 to 80 MPa $\sqrt{\text{m}}$  produced only 70  $\mu\text{m}$  of HEAC calculated from dcPD measurements, and the crack branched with further loading. The fracture surface was oxidized, prohibiting a precise correlation of actual crack length to dcPD calculations. However, the location of the onset of crack branches shown in Figure 3 accurately coincides with the dcPD-measured extent of slow cracking prior to the onset of the Stage III behavior (Figure 2). The tearing above 80 MPa $\sqrt{\text{m}}$  produced a unique fracture surface, shown in Figure 2b, unlike the ductile microvoids typical of fracture in air for this steel; however, this is not definitive since the surfaces were damaged from corrosion that occurred post-fracture.

AerMet™ 100 specimens aged at 482°C and 510°C showed transgranular HEAC, as well as some macroscopic crack branching, when stressed in NaCl solution at  $E_{App}$  of  $-0.9 V_{SCE}$ . Fractographs are presented in Figure 4. These two temperatures showed essentially identical fracture surface features. Evidence of martensite lath interface cracking is prominent when aged at 510°C (Figure 3b), and is virtually identical to the fractographs obtained for severe IHAC<sup>[1]</sup> and HEAC<sup>[2]</sup> of this steel aged at 482°C.

HEAC was predominantly intergranular for the specimen aged at 538°C (Figures 4c and d). Such prominent IG cracking has not been observed previously in IHAC or HEAC of AerMet™ 100, although partial-minority features of IG HEAC have been noted<sup>[2,13,19]</sup>. Previous reports of IG HEAC of AerMet™ 100 always coincided with crack branching<sup>[2,13,19]</sup>, while such branching was not observed for this specimen aged at 538°C. Both TG and IG HEAC of this steel at various aging conditions (Figures 3 and 4) were very different from the microvoid morphology typical of fracture in moist air. Key experimental results for each aging condition stressed under this electrochemical condition are summarized in Table 3.

### III.C. Effect of Aging on HEAC at $E_{App} = -0.625 V_{SCE}$

A second set of experiments were conducted at  $E_{App}$  of  $-0.625 V_{SCE}$ , a potential which previously gave the highest HEAC resistance for the 482°C temper explained based on electrochemically limited H production and uptake at the crack tip<sup>[2]</sup>. Experimental findings are summarized in Figure 5 and Table 4. The initial crack size for each specimen was essentially identical, however the loading rate was slower for the 510°C age. When aged at 510°C, the operationally defined  $K_{TH}$  decreased to 30.6 MPa√m (24% of  $K_{IC}$ ), compared to higher  $K_{TH}$  of 40.8 MPa√m for the microstructure aged at 482°C. Unexpectedly, the AQ condition produced the lowest  $K_{TH}$  at 20 MPa√m (16% of  $K_{IC}$ ), although this specimen showed the highest  $K_{TH}$  for  $E_{App}$  of  $-0.9 V_{SCE}$  (Figure 1). This reversal of HEAC resistance is possibly due to the shorter precrack used for the experiment at  $-0.625 V_{SCE}$ , and will be discussed later. Additionally, the exact value of  $K$  at initiation of HEAC may be masked due to slow crack growth in the vicinity of the dcPD resolution limit, and the operationally defined  $K_{TH}$  values reported here do not necessarily represent the true threshold<sup>[2]</sup>. If the alternate measurement of susceptibility,  $K_{TH}^*$ , is used, the AQ condition still has the lowest  $K_{TH}^*$ , although the trend reverses for the 482°C and 510°C aging temperatures, as shown in Figure 5.

Rates of HEAC measured at  $-0.625 V_{SCE}$  are low and to a first approximation comparable for all aging conditions, as shown in Figure 6. These crack growth rate results are generally similar in that  $da/dt$  values are low compared to HEAC at  $-0.900 V_{SCE}$ . In Figure 6 the Stage-I growth regime is obscured by the resolution limit of the dcPD system and is not observable for any heat treatment with the possible exception of the AQ condition. Reasonably constant  $da/dt$  with increasing  $K$  ( $da/dt_{II}$ ) is not strongly apparent, again with the possible exception of the AQ condition. Approximate  $da/dt_{II}$  values for  $K$  of about  $35 \text{ MPa}\sqrt{\text{m}}$  are shown in Figure 5 and Table 4. Differentiation of true microstructurally based differences in slow crack growth rates, typical of this regime of low-electrochemical H uptake and in the range below about  $2 \text{ nm/s}$ , is challenging. Insufficient experiments were conducted to achieve definitive results. The rapidly increasing  $da/dt$  at high  $K$  (above  $50$  to  $80 \text{ MPa}\sqrt{\text{m}}$ ) may represent Stage-III growth and perhaps H interaction with microvoid fracture processes.

#### III.D. Effect of Aging Temperature on HEAC Morphology at $E_{App} = -0.625 V_{SCE}$

Subcritical HEAC was confirmed by SEM analysis for each aging condition of AerMet™ 100 stressed at this near-free corrosion potential; the HEAC fracture mode was TG for all tested heat treatments as shown in Figure 7. The TG features were similar in the  $482^\circ\text{C}$  and  $510^\circ\text{C}$  temper (Figures 7c and d), where the crevices in the latter image was caused by removing the corrosion damage. However, the fracture in the AQ condition (Figures 7a-b and 8) was dissimilar, showing a flatter, rounder variation of transgranular cracking. Some martensite plate cracking is observed (arrow in Figure 7b), but not as dominant nor common as those found in the  $482^\circ\text{C}$  age. Some dimples are visible even at low magnification, possibly showing cracking at the larger carbide. Overall, the cracking does not appear to be restricted to martensite plate and packet boundaries as it did in the other two aged specimens, and there are larger areas of completely flat fracture (Figure 7a and b).

The low magnification SEM image for the AQ specimen, Figure 8, shows that HEAC occurred, but the extent was limited. This particular specimen was fatigued to fracture after HEAC testing, thus clearly indicating the exact extent of HEAC. Of the  $240 \mu\text{m}$  total crack growth, the crack only advanced  $35\sim 50 \mu\text{m}$  upon loading to  $K$  of  $40 \text{ MPa}\sqrt{\text{m}}$ , based on dcPD measurements. The dcPD calculated crack growth was approximately 15% higher than measurements from the SEM image (Figure 8); most of the error is likely due to high  $K$  loading

(above 130 MPa $\sqrt{m}$ ) which caused some plastic deformation induced dcPD signals. The rest of the crack growth is related to the Stage-III behavior shown in Figure 6. Comparing the AQ and 510°C conditions, the reduction in  $da/dt_{II}$  with increased aging temperature was barely an order of magnitude, as shown in Figure 6 and Table 4. A factor-of-three difference is confirmed based on fractographic measurements; a 140 h test produced only 240  $\mu\text{m}$  of total-SEM measured crack growth for 510°C, compared to the same amount of SEM observed cracking (Figure 8) in the AQ condition stressed for 44 h.

**Table 4. Summary of HEAC results for  $E_{\text{App}} = -0.625 V_{\text{SCE}}$**

Heat Treatment	$a_0$ (mm)	Initial $dK/dt$ (MPa $\sqrt{m}/h$ )	$K_{\text{TH}}$ (MPa $\sqrt{m}$ ) [Figure 5]	$K_{\text{TH}}^*$ (MPa $\sqrt{m}$ ) [Figure 5]	$da/dt_{II}$ (nm/s) [Figure 6]	Fracture Mode [Figures 7 and 8]
AQ	0.81	$1.8 \times 10^{-3}$	40.8	19.3	$\sim 1.5$	TG
482°C	0.95	$1.9 \times 10^{-3}$	20	22.3	$\sim 0.9$	TG
510°C	0.78	$8.3 \times 10^{-5}$	30.6	67	$\sim 0.4$	TG

## IV. Discussion

### IV.A. Effect of Aging Temperature on HEAC of AerMet<sup>TM</sup> 100

Over the aging temperature range of 482°C to 538°C, AerMet<sup>TM</sup> 100 is susceptible to severe transgranular HEAC when stressed in neutral 3.5% NaCl at  $E_{\text{App}}$  of  $-0.9 V_{\text{SCE}}$ . The  $K_{\text{TH}}$  values are between 13 to 23 MPa $\sqrt{m}$ , which is only a small fraction of  $K_{\text{IC}}$ . The severe reduction in cracking resistance remains significant for AerMet<sup>TM</sup> 100 aged to retain  $K_{\text{IC}}$  above 110 MPa $\sqrt{m}$  and  $\sigma_{\text{YS}}$  above 1300 MPa. As shown in Table 2, the highest strength/toughness combination is obtained when optimally aged at 482°C. However, this temper showed exceptionally severe IHAC and HEAC susceptibility, and it was speculated that modifications to heat treatment could reduce the severity by  $M_2C$  coarsening<sup>[2]</sup>. Tempering at 510°C provides only a small reduction in yield strength while retaining the fracture toughness, while the microstructure offers a higher volume fraction of  $M_2C$  with less coherent interfaces that presumably yield a higher H-trap binding energy<sup>[6]</sup>. This increased binding energy was

anticipated to increase HEAC resistance by preferentially trapping H away from the fracture site. Unfortunately, Figure 9 shows virtually no difference in HEAC response stressed at  $E_{App}$  of  $-0.9 V_{SCE}$  (and only a modest reduction in crack growth rates at  $-0.625 V_{SCE}$ ). However, substantial resistance to HEAC was found in the as-quenched condition, with  $K_{TH}$  above  $80 \text{ MPa}\sqrt{\text{m}}$ , for the severe hydrogen environment condition of  $-0.9 V_{SCE}$ . The improvement in  $K_{TH}$  is partially attributed to the decreased  $\sigma_{YS}$  (Figure 5), which is known to improve HEAC resistance in many steels<sup>[3,20]</sup>. However, 400 MPa reduction in  $\sigma_{YS}$  alone cannot account for the 4-fold increase in  $K_{TH}$  or  $K_{TH}^*$ . Moreover,  $\sigma_{YS}$  is approximately equal for the 538°C age and AQ condition; the measured differences in  $K_{TH}$  and  $da/dt_{II}$  are undoubtedly due to the microstructure-H interactions that govern HEAC.

Polarization to  $-0.625 V_{SCE}$  resulted in improved resistance to HEAC of AerMet™ 100, paralleling the behavior of the optimally aged (482°C) microstructure<sup>[2]</sup>. A typical example is presented in Figure 9. For  $E_{App}$  of  $-0.625 V_{SCE}$ ,  $K_{TH}$  and  $da/dt_{II}$  varied less significantly across the tempering conditions than at  $-0.9 V_{SCE}$ . The general dependence was reversed, with lowest values of  $K_{TH}$  at the AQ condition and highest  $K_{TH}$  aged at 482°C. This is unexpected from the yield strength correlation, which predicts better HEAC resistance with decreasing strength<sup>[3]</sup>. However, when  $da/dt_{II}$  or  $K_{TH}^*$  is used as the benchmark, the highest resistance is found when aged at 510°C. Speculatively, crack tip H production for  $E_{App}$  of  $-0.625 V_{SCE}$  is already very low, which obscured the effect of microstructure on HEAC behavior as measured by  $K_{TH}$  or  $K_{TH}^*$ . The fact that the AQ condition has the lowest  $K_{TH}$  or  $K_{TH}^*$  at this applied potential is significant considering the best resistance it displayed at  $E_{App}$  of  $-0.9 V_{SCE}$ . The exact values of  $K_{TH}$  and  $K_{TH}^*$  shown in Figure 5 and Table 4 may not accurately describe the true threshold and it is possible that cracking will occur below the operationally defined thresholds. Problems were also encountered in carrying out these complex HEAC experiments and additional work is required to define the behavior of the AQ condition. Such work is significant to mechanism interpretation, but not alloy development since secondary hardening carbides are critical to strength/toughness combinations required for steels such as AerMet™ 100.

In terms of  $da/dt_{II}$ , HEAC resistance measured for  $E_{App} = -0.9 V_{SCE}$  was virtually identical in all three aged conditions. This is particularly evident between the 482°C and 510°C conditions as shown in Figure 2. Since the intergranular crack path was dissimilar for the 538°C case, it is probably coincidental that  $da/dt_{II}$  for that temper matches those of the other two that

exhibited transgranular cracking. These results suggest that  $M_2C$  coarsening by aging at  $510^\circ\text{C}$  has not sufficiently increased the H binding energy to the precipitates ( $E_B = 11 \text{ kJ/mol}$  at  $482^\circ\text{C}$ ) to equal or exceed the binding energy characteristic of martensite interfaces ( $61 \text{ kJ/mol}$ )<sup>[5]</sup>. As such, H diffusing from the crack tip surface to the high stress region within the fracture process zone will preferentially partition from the carbides to martensite interfaces due to the large binding energy difference for both aging conditions; a dramatic improvement in HEAC resistance is thus not achieved. Considering the possibility of more modest changes in cracking resistance with aging, diffusion limited  $da/dt_{II}$  is related to the effective H diffusivity,  $D_{H,eff}$ , a characteristic distance,  $X_C$ , and surface hydrogen concentration in equilibrium with crack tip overpotential,  $C_s$ , in the following form<sup>[21]</sup>:

$$da/dt_{II} = \frac{D_{H,eff}}{X_C} f(C_s, C_{crit}) \quad [1]$$

where  $f(C_s, C_{crit})$  is a functional description of the boundary conditions for H-diffusion and  $C_{crit}$  is the critical amount of H required at the crack nucleation site for H damage to form. As a first approximation, it is reasonable to assume based on the form of Equation 1 that  $da/dt_{II}$  is proportional to the product of  $D_{H,eff}$  and  $C_s^2$ <sup>[21]</sup>. The hypothesis is that  $D_{H,eff}$  decreases and  $C_s$  increases as the  $M_2C$  carbides lose coherence with increasing aging temperature from  $482$  to  $510^\circ\text{C}$ . This behavior is due to increasing H-trap binding energy as the coherence of  $M_2C$  interfaces decreases. The implication from the data is that constant  $da/dt_{II}$  with aging means that the trap-induced changes in the magnitude of decreasing  $D_{H,eff}$  and increasing  $C_s^2$  are essentially offsetting.

Other terms in Equation 1 must be considered. The critical distance  $X_C$  is closely related to the stress distribution in the crack tip process zone which in turn is governed by alloy flow strength and work hardening<sup>[3,21]</sup>. It is reasonable to assume that these factors are affected to a secondary extent by aging between  $482^\circ\text{C}$  and  $510^\circ\text{C}$ . It is possible that  $C_{crit}$  changes with aging. This critical concentration depends on the local normal stress acting on this H-laden site as well as the atomic details of the interface or lattice. For HAC in AerMet<sup>TM</sup> 100, results suggest that martensite lath and/or packet boundaries constitute this damage site and crack path<sup>[1,2]</sup>. There is no documented reason to believe that the local stress, trapped H content, and atomic environment of these martensite interfaces change with aging between  $482$  and  $510^\circ\text{C}$ . Of course, subtle

differences may exist but have not been elucidated. Finally, it is possible that Equation 1 does not fully describe  $da/dt_{II}$  if the  $C_S$  crack surface boundary condition is surface reaction rate limited<sup>[3]</sup>.

Considering the AQ condition,  $da/dt_{II}$  was substantially slower at  $-0.9 V_{SCE}$  (Figure 2) and the microscopic mode of HEAC was different from transgranular martensite interface cracking due to trapped H (Figures 3 and 4). Following the logic associated with H diffusion limited  $da/dt_{II}$ , in the absence of  $M_2C$  carbides and precipitated austenite,  $D_{H,eff}$  is expected to be substantially higher compared to the aged conditions. However,  $C_S$  will be proportionately lower and the change in the terms  $D_{H,eff}$  and  $C_H^2$  is unknown but may be reasonably similar for AQ and the aged microstructures. The martensite should be of similar morphology and have unrecovered dislocation structure for both the as-quenched and aged conditions; thus the strong difference in HEAC resistance is not easily understood. Perhaps short range segregation is enabled by aging near  $500^\circ C$  to promote martensite interface decohesion in concert with trapped H. It is also possible that HEAC was promoted by increased crack tip stresses from the strength increase during aging, compared to the lower strength AQ condition, although severe HEAC produced for the  $538^\circ C$  age of AerMet<sup>TM</sup> 100 somewhat weakens this explanation. Also, it is likely that crack tip stresses are not substantially different for the different microstructures examined due to the fact that increased work hardening preferentially elevates crack tip stresses for the AQ (and  $538^\circ C$ ) microstructures to offset reduced  $\sigma_{YS}$ .

These complications aside, the present results show that the as-quenched martensitic microstructure is not, per se, uniquely embrittled by H. Some aspect of aging must promote HEAC based on the results shown in Figures 2 through 4. Thermal desorption spectroscopy (TDS) results show dramatic differences in the trapping situation, for AQ vs. the  $482^\circ C$  age of AerMet<sup>TM</sup> 100, but only for the H outgassing peak characteristic of the lack of  $M_2C$ <sup>[5]</sup> and consistent with the above discussion. Subtle differences in H trapping were suggested by the desorption peak structure generally associated with martensite and undissolved TiC interface traps states. However, this behavior was not investigated in detail and additional experiments are required.

While H diffusion limitation of  $da/dt_{II}$ , coupled with H decohesion and trapping, provides a reasonable framework to examine the results of the present experiments, it is not possible to explain the observed microstructural effects. It is reasonable to speculate that  $da/dt_{II}$  values are

diffusion rate limited, as described by Equation 1, and the aging independence is traced to offsetting effects of trapping on H solubility and diffusivity. The magnitude of these effects are not known at present, but can be assessed based on the results of TDS experiments<sup>[5]</sup>. Such measurements, coupled with improved modeling of the threshold and kinetics of HEAC, are required to provide a fundamentally grounded basis for alloy and process development to mitigate IHAC and HEAC.

#### IV.B. Loading Rate and Crack Size Effects

Because changes in heat treatment affect yield strength, precrack length was increased to maintain small-scale yielding at high applied  $K$  for each condition. The loading rate was accordingly modified to maintain an approximately constant  $dK/dt$  and the test conditions are listed in Tables 3 and 4. In one specimen ( $E_{App} = -0.625 V_{SCE}$ , 510°C age), the loading rate was purposefully lowered to observe any possible effects on HEAC response. The slower loading rate resulted in higher  $K_{TH}^*$  and slower  $da/dt_{II}$  when comparing 482°C and 510°C at  $E_{App}$  of  $-0.625 V_{SCE}$ , whereas the opposite trend is expected for loading-rate affected results<sup>[1-3,22]</sup>. The variations in loading rate presumably did not affect the results.

Due to occluded crack geometry, different crack lengths may produce different HEAC behavior<sup>[23,24]</sup>. In the range of crack sizes examined (0.3 ~ 3 mm), there is some evidence of adverse effects for cracks shorter than 1 mm<sup>[24]</sup>. Given the small differences between the 240  $\mu\text{m}$  and 950  $\mu\text{m}$  precracks in the 482°C temper,  $K_{TH}$  and  $da/dt_{II}$  are not likely affected. Additionally, previous findings suggest that long precracks (1 ~ 3 mm) show no variances in observed  $K_{TH}$ <sup>[24]</sup>. Overall, loading rate and crack size effects were not evident in the results.

#### IV.C. Intergranular HEAC Aged at 538 °C

Instances of intergranular fracture were rare in HEAC<sup>[2]</sup> and IHAC<sup>[1]</sup> of peak-toughness AerMet<sup>TM</sup> 100. However, aging at 538°C produced predominantly IG HEAC at  $E_{App}$  of  $-0.9 V_{SCE}$ . Since the specimens used for the IHAC<sup>[1]</sup>, HEAC<sup>[2]</sup> and current experiments were cut from the same small forging of AerMet<sup>TM</sup> 100, the composition should be virtually identical across all the experiments. Assuming no significant segregation during forging, the onset of IG fracture mode must be attributed to changes in microstructure due to aging at 538°C. This assumption is substantiated since IG fracture on this specimen was not localized but prevalent across the entire fracture surface (Figure 4d). Uniform IG fracture was not observed on any

other experiments<sup>[1,2]</sup> or by any other observers<sup>[13-15,19,25]</sup> who focused on AerMet™ 100 aged at 482°C. It is unlikely that *localized* segregation can be responsible for such IG cracking.

Large-scale impurity segregation to prior austenite grain boundaries is a commonly cited reason for IG HAC in less pure and lower alloy content high strength steels<sup>[3,26]</sup>. For high strength tempered martensitic microstructures in general, H-free toughness is degraded by tempering in the range from 250°C to 450°C, traced to impurity (P in particular) segregation to prior austenite boundaries coupled with cementite precipitation at martensite interfaces<sup>[26]</sup>. Susceptibility to HEAC due to H-impurity interaction has been characterized by an impurity-weighted composition parameter ( $\psi = \text{Mn} + 0.5 \text{ Si} + \text{S} + \text{P}$  in weight %)<sup>[20]</sup>. While cementite precipitation in the range of 400°C degrades the toughness of AerMet™ 100<sup>[6,7]</sup>, IG fracture with or without H is not expected for AerMet™ 100 given its very low  $\psi$  (0.029 wt%)<sup>[2]</sup>. Impurity segregation is thermally activated and exhibits classic “C-curve” time-temperature kinetics<sup>[26]</sup>. If the critical temperature range for optimal segregation lies above 510°C, it is possible that the low bulk concentration of impurities could sufficiently segregate at higher aging temperatures such as 538°C to enable IG HEAC, while not doing so at 482°C. This application of the classic impurity-H interaction mechanism requires confirmation of segregation by Auger spectroscopy and such results have not been reported for high purity ultra-high strength steels<sup>[26]</sup>.

Given the high H-binding energy at both martensite boundaries and prior austenite grain boundaries, H will accumulate to very high concentrations at both trap sites. Previously, it was speculated that the H-degraded strength of the grain boundary of this steel was higher than the equivalently H-reduced martensite boundary strength<sup>[2]</sup>. Otherwise, IG cracking is expected at the peak-toughness age. In this view, the fracture mode transition from TG to IG can be due to weakened grain boundaries, strengthened martensite boundaries, or both, upon aging at the higher temperature. The fact that  $K_{\text{TH}}$  was higher than the 482°C and 510°C values but still low (23 MPa $\sqrt{\text{m}}$ ) suggests increased martensite boundary strength. However,  $K_{\text{TH}}$  was much higher in the AQ condition and cracking was not IG, which suggests weakened grain boundary strength at 538°C.

Aging at 538°C produces three significant changes to microstructure from the 482°C and 510°C ages;  $\text{M}_2\text{C}$  coarsening and loss of coherency with the matrix, increased  $\gamma'$  precipitation and intra-martensite plate  $\gamma'$  precipitation. There was no evidence of preferred  $\text{M}_2\text{C}$  precipitation on martensite boundaries or prior austenite grain boundaries at any aging temperature, so the

changes in  $M_2C$  characteristics are unlikely to directly cause grain boundary weakening or martensite boundary strengthening. Conversely,  $\gamma'$  was reported to precipitate on martensite plate boundaries. Increased  $\gamma'$  precipitation can increase the H-degraded fracture strength of the martensite plate interface by one of two hypothetical mechanisms: prohibiting the martensite transformation of  $\gamma'$  or restricting a connected martensite lath crack path.

In the presence of H it was speculated that thin-film  $\gamma'$  transforms to martensite by H-stress interactions to promote HEAC along martensite boundaries<sup>[2,27,28]</sup>. Given the composition of  $\gamma'$  (30 wt. % Ni) in AerMet™ 100, it is unlikely to transform to martensite in its bulk form even with elevated stresses near the crack tip; thus a thin-film-specific mechanism was hypothesized<sup>[27,28]</sup>. Within their framework, discontinuous distribution of thin-film  $\gamma'$  is necessary for such transformation, and networked distribution of thicker  $\gamma'$  prohibits that transformation. If this mechanism actually facilitates TG HEAC at the peak toughness temper, then IG cracking in the 538°C age can be attributed to increased  $\gamma'$  precipitation which is less likely to transform to martensite. That assumes that the HEAC fracture site for the 482°C and 510°C to be the interface between martensite and  $\gamma'$ . On the other hand, if the martensite-martensite interfaces are responsible for low  $K_{TH}$  HEAC, then the presence of intra-lath  $\gamma$  and increased  $\gamma$  precipitation would reduce the percentage of such boundaries by precluding direct contact between two martensite plates. Furthermore, with sufficient precipitation,  $\gamma'$  may prevent "clean" martensite plate crack paths from connecting. Aging for 5 h at 538°C produces at least 5.5%  $\gamma$  and partially interconnected  $\gamma'$  (Figure 10)<sup>[6]</sup>.

$M_2C$  coarsening can indirectly increase the martensite boundary strength by the previously proposed mechanism of preferential H trapping<sup>[2]</sup>. If the binding energy of  $M_2C$  carbides is increased by particle coarsening and the distribution remains relatively uniform throughout the microstructure, then  $M_2C$  carbides can act as preferential traps to keep H away from potential fracture sites such as martensite plate boundaries. Since tempering at 538°C produces incoherent and presumably increased  $E_B$  of these carbides, this mechanism may be responsible for the lack of martensite lath cracking.  $M_2C$  coarsening does not increase the H-reduced fracture strength of the martensite laths; instead it reduces the amount of H accumulation at those sites. However, this is speculative since IG HEAC occurs at this temper at relatively low  $K_{TH}$ , and the only reasonable explanation is arbitrary: that low concentrations of H, after partitioning to incoherent  $M_2C$ , weakens the austenite grain boundaries more than the martensite

boundaries.

Alternatively, the increased aging temperature may change the grain boundary composition to lower the H-reduced fracture strength of the grain boundary. As mentioned previously, the changes in microstructure from 482°C to 538°C are limited to  $M_2C$  and  $\gamma'$ . The composition of those features change, but the differences are mild (less than 10%) and only involve elements (Cr, Mo, Fe, Co and Ni) that are not traditionally considered to be grain boundary embrittlors<sup>[20]</sup>. However, the grain boundary composition has not been measured and the possibility remains for low temperature diffusion of S and P<sup>[3,26]</sup>.

#### IV.D. $K_{TH}$ and $da/dt_{II}$ in the As-Quenched Condition

The HEAC mode of non-aged AerMet<sup>TM</sup> 100 is unique from the aged specimens, as shown in Figures 3, 7a-b and 8. There are no IG features, and martensite lath/packet interface cracking found in peak-aged IHAC<sup>[1]</sup> and HEAC<sup>[2]</sup> are not prevalent. These features support the  $\gamma'$ -martensite transformation induced HEAC mechanism for aged conditions, as the non-aged specimen (0%  $\gamma'$ ) produced substantially higher  $K_{TH}$  and lacked widespread indications of martensite boundary cracking when stressed at  $E_{App}$  of  $-0.9 V_{SCE}$ . Regardless of the exact mechanism, the experimental results show that thin film interlath reverted austenite, while increasing the H-free fracture toughness of AerMet<sup>TM</sup> 100, substantially reduces its HEAC resistance. Alternatively, the  $M_2C$  carbides that were anticipated to increase HEAC resistance may actually increase the susceptibility by somehow enhancing the fracture site H concentration. This alternative theory has not been developed.

When stressed at  $E_{App}$  of  $-0.625 V_{SCE}$ , the AQ condition actually shows the lowest  $K_{TH}$  and  $K_{TH}^*$ . It seems particularly strange that the  $K_{TH}$  is lower at  $E_{App} = -0.625 V_{SCE}$  compared to  $-0.9 V_{SCE}$ . Close examination of the fractographs (Figures 3, 7 and 8) and crack growth curves (Figures 2 and 6) shows the onset of Stage III growth around 40 MPa $\sqrt{m}$  for  $E_{App} = -0.625 V_{SCE}$  and 100 MPa $\sqrt{m}$  for  $E_{App} = -0.9 V_{SCE}$ . Stage-III behavior depends on loading rate, and it is possible that the differences in operational threshold are affected by the early onset of atypical Stage III crack growth behavior. As it was shown previously<sup>[2]</sup>, very slow crack kinetics could hinder the determination of exact values for  $K_{TH}$ . Presumably, the actual threshold lies

---

<sup>1</sup> Although there is some evidence of retained austenite in the non-aged condition[10], reverted austenite does not exist in the AQ condition. Furthermore, retained austenite does not have thin-film interlath morphology.

somewhere in the range of 20 to 87 MPa $\sqrt{m}$ .

Uncertainties in the exact value of  $K_{TH}$  and  $K_{TH}^*$  are not critical to the interpretation of aging effects on HEAC as long as the trend is accurate. It is clear from the fractographic results that HEAC cracking in the AQ condition is limited when compared to aged specimens. Moreover, the interpretations of microstructural effects on the HEAC response at  $E_{App}$  of  $-0.9 V_{SCE}$  are valid for the AQ condition. The  $da/dt_{II}$  is under 2 nm/s for the AQ microstructure at both potentials. Since both  $\gamma'$  and  $M_2C$  are suspected to slow H diffusion, their absence is expected to increase the crack growth rate, as observed in Figure 6.

Lastly, aging duration is a critical variable that has not been investigated in these experiments. Aging time has a pronounced effect on microstructure, particularly affecting the size and coherence of  $M_2C$  carbides and volume fraction of  $\gamma'^{[9]}$ . For example, up to 23 vol. % of  $\gamma'$  was formed when aged at 482°C for 100 h compared to a near-0 volume fraction for 5 h<sup>[9]</sup>. Small differences in aging time can easily alter these properties, especially at the early stages (below 10 h). If the HEAC response to microstructural differences are as sensitive results show, additional studies for isothermal aging effects on HEAC are required.

## V. Conclusions

1. When aged to obtain high strength ( $\sigma_{YS} > 1300$  MPa) and plane strain fracture toughness ( $K_{IC} > 100$  MPa $\sqrt{m}$ ), at several different aging temperatures, AerMet™ 100 is similarly susceptible to severe hydrogen environment assisted cracking in neutral 3.5% NaCl and at an applied potential of  $-0.9 V_{SCE}$ . This is quantified by two parameters: reduced threshold stress-intensity for HEAC,  $K_{TH}$ , to as low as 10% of  $K_{IC}$ , and subcritical Stage-II crack growth rate,  $da/dt_{II}$ , as high as 30 nm/s.
2. The aging independence of HEAC at  $-0.9 V_{SCE}$  may be consistent with a mechanistic explanation based on H diffusion control of crack growth rate, but material dependent terms in the model for  $da/dt_{II}$  and the very detail of the model remain uncertain. It is not possible to design alloy composition and processing conditions based on such existing models.

3. Qualitatively, increasing incoherence of  $M_2C$  precipitates does not result in reduced  $da/dt_{II}$ , perhaps due to the counterbalancing effects of increased trapping; causing reduced H diffusivity but increased H solubility; as suggested by the diffusion model. Relatively low H-trap binding energy of these precipitates for the tempers examined prevents beneficial shielding of H partition to martensite lath/packet boundary interfaces where such segregation enables decohesion.
4. When aged at 538°C for 5 h, the HEAC fracture mode is predominantly intergranular at an applied potential of  $-0.9 V_{SCE}$ . Hydrogen cracking was transgranular at all other aging conditions for  $E_{App} = -0.9 V_{SCE}$ , similar to the behavior of optimally aged (482°C) AerMet™ 100. It is suggested that precipitation of intra-plate austenite at 538°C impedes fracture along martensite boundaries, promoting the less favorable intergranular crack path at higher  $K_{TH}$ .
5. In the as-quenched condition, susceptibility to HEAC at  $-0.9 V_{SCE}$  is substantially reduced, with  $K_{TH}$  of up to 70% of  $K_{IC}$  and slow  $da/dt_{II}$  of 1 nm/s. The fracture path is transgranular, but not limited to martensite plate boundary cracking as observed in IHAC and HEAC of the peak-aged condition. Speculatively, the lack of thin-film reverted austenite increases the  $K_{TH}$  as it otherwise aids martensite plate boundary cracking; but the lack of uniformly distributed  $M_2C$  carbides slightly increases  $da/dt_{II}$  due to increased effective H diffusivity not offset by reduced H solubility.
6.  $K_{TH}$  and  $da/dt_{II}$  levels for HEAC at an applied potential of  $-0.625 V_{SCE}$  are similar for the as-quenched and 482°C and 510°C aging temperatures. Notably, each aging condition shows a greatly reduced HEAC susceptibility, as established previously for optimally aged AerMet™ 100. The combination of alternate aging temperatures and optimal electrochemical polarization did not produce immunity to HEAC.
7. The improved purity of AerMet™ 100 does not provide immunity to IG HEAC. However, the increased purity may raise the  $K_{TH}$  required for IG fracture, causing TG fracture to be favored for optimally aged AerMet™ 100.

## Figures

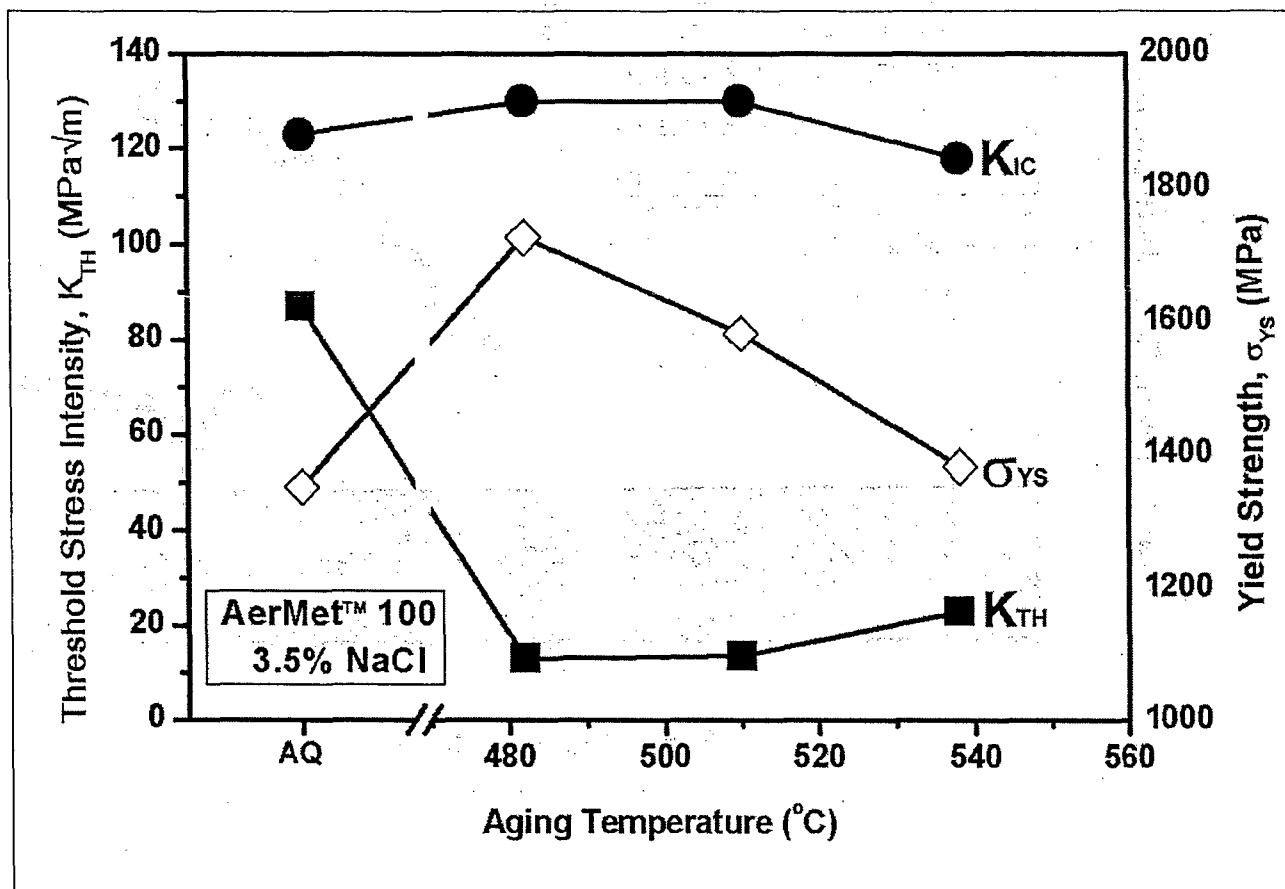


**Figure 1** Threshold stress intensity,  $K_{TH}$ , vs. aging temperature for AerMet<sup>TM</sup>100 stressed under slow-rising crack mouth opening displacement at  $E_{App}$  of  $-0.9 V_{SCE}$  in neutral 3.5 % NaCl. Literature reported  $K_{IC}$  and  $\sigma_{YS}$  values for each tempering condition in Table 2 are displayed for reference.

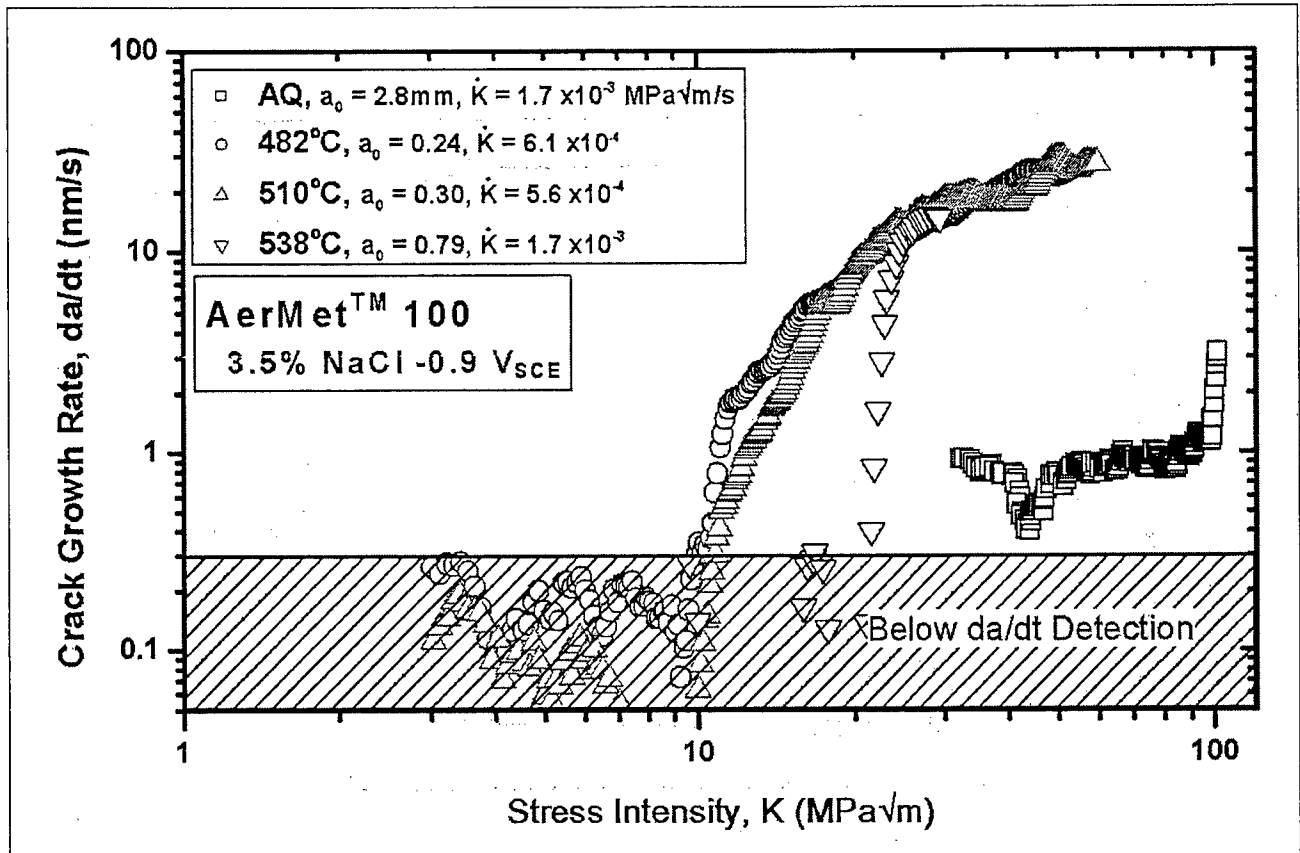


**Figure 2** Subcritical crack growth rate vs.  $K$ , for various aging temperatures of AerMet™ 100 stressed under constant grip displacement rate in 3.5 % NaCl at  $E_{App}$  of  $-0.625 V_{SCE}$ . The initial loading rate,  $dK/dt$ , and fatigue precrack length for each condition are noted. Load and dcPD data were not collected for the AQ condition at  $K$  less than  $30 \text{MPa}\sqrt{\text{m}}$ .

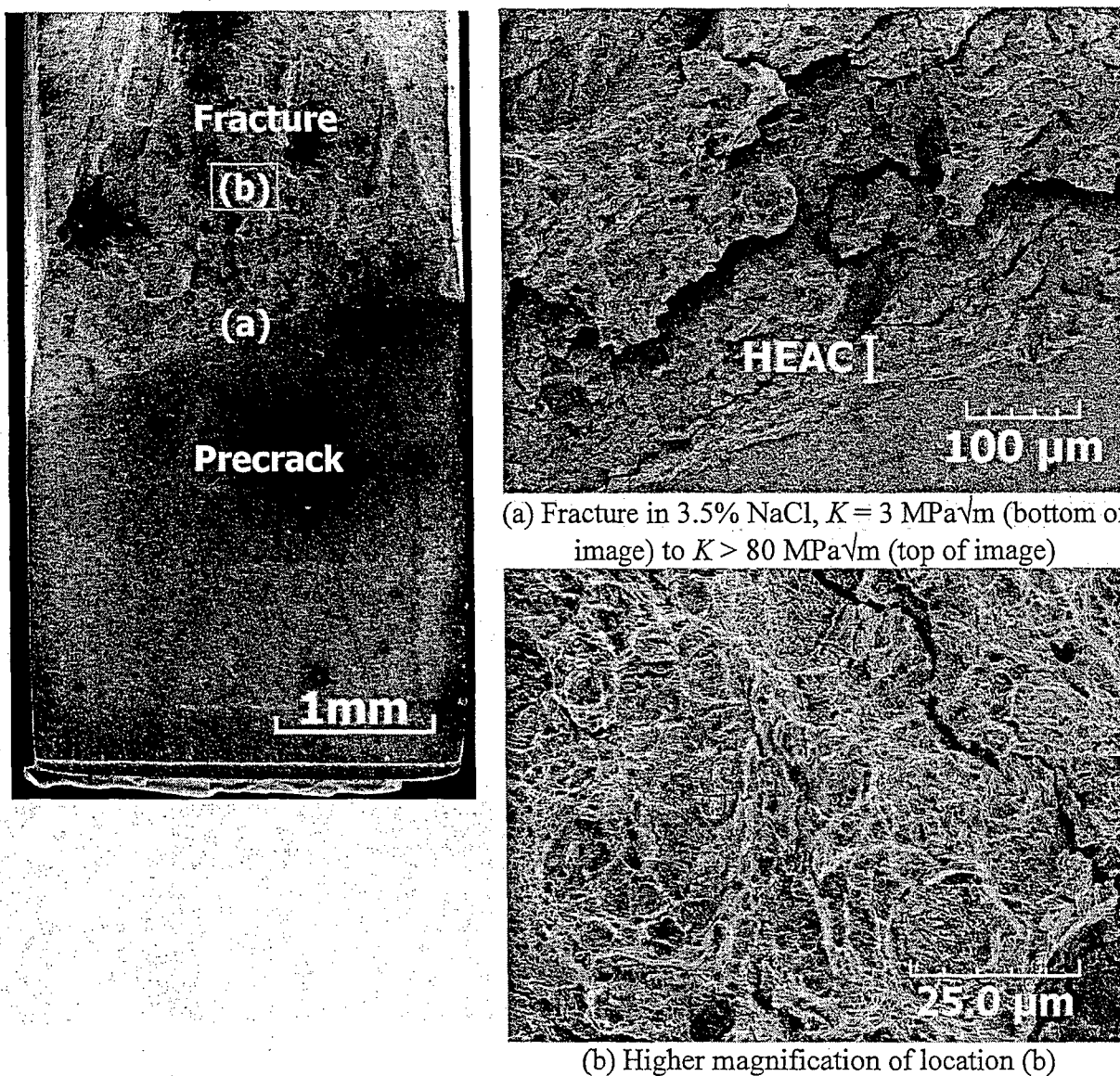


**Figure 3** Scanning electron fractographs of the fracture surface of an as-quenched (AQ) AerMet™ 100 specimen fractured in 3.5% NaCl ( $-0.900 V_{SCE}$ ). The SEM image on the left shows the macroscopic appearance. The black spots on the left image are due to oxidation. (a) shows a small region marked "HEAC" that represents HEAC crack growth of  $70 \mu\text{m}$  over the loading range from  $K$  of 3 to  $80 \text{ MPa}\sqrt{\text{m}}$ . Above  $80 \text{ MPa}\sqrt{\text{m}}$ , extensive crack branching is evidenced and presumably H assisted since  $K_{IC}$  equals  $123 \text{ MPa}\sqrt{\text{m}}$  from Table 2. (b) shows the typical appearance of high  $K$  (above  $80 \text{ MPa}\sqrt{\text{m}}$ ) cracking in this condition.

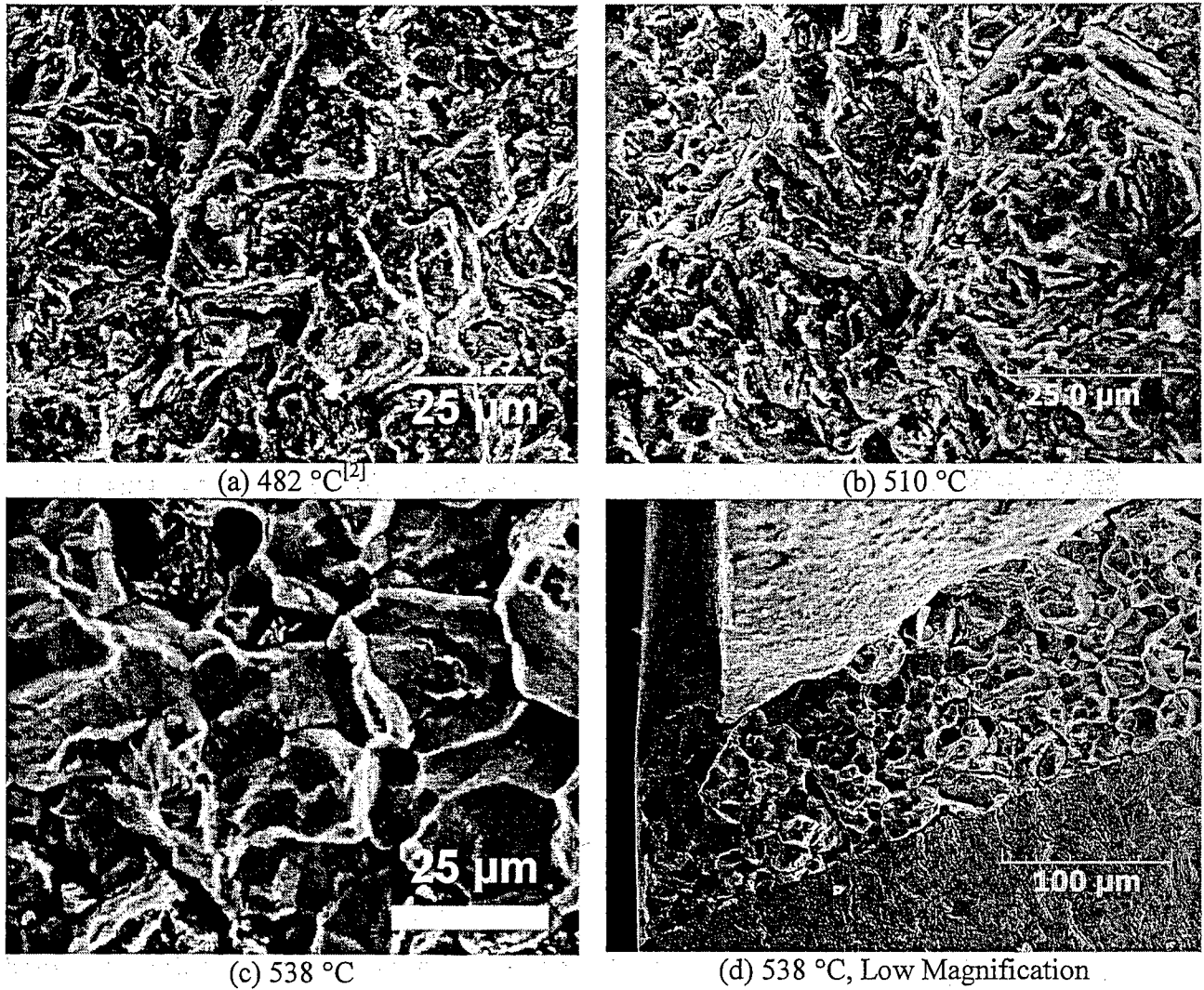


**Figure 4** SEM images of hydrogen affected fracture surfaces for various aging temperatures of AerMet™ 100 stressed in 3.5% NaCl at an applied potential of  $-0.9 V_{SCE}$ . (a) and (b) show predominantly transgranular fracture, while (c) and (d) shows predominantly intergranular fracture.

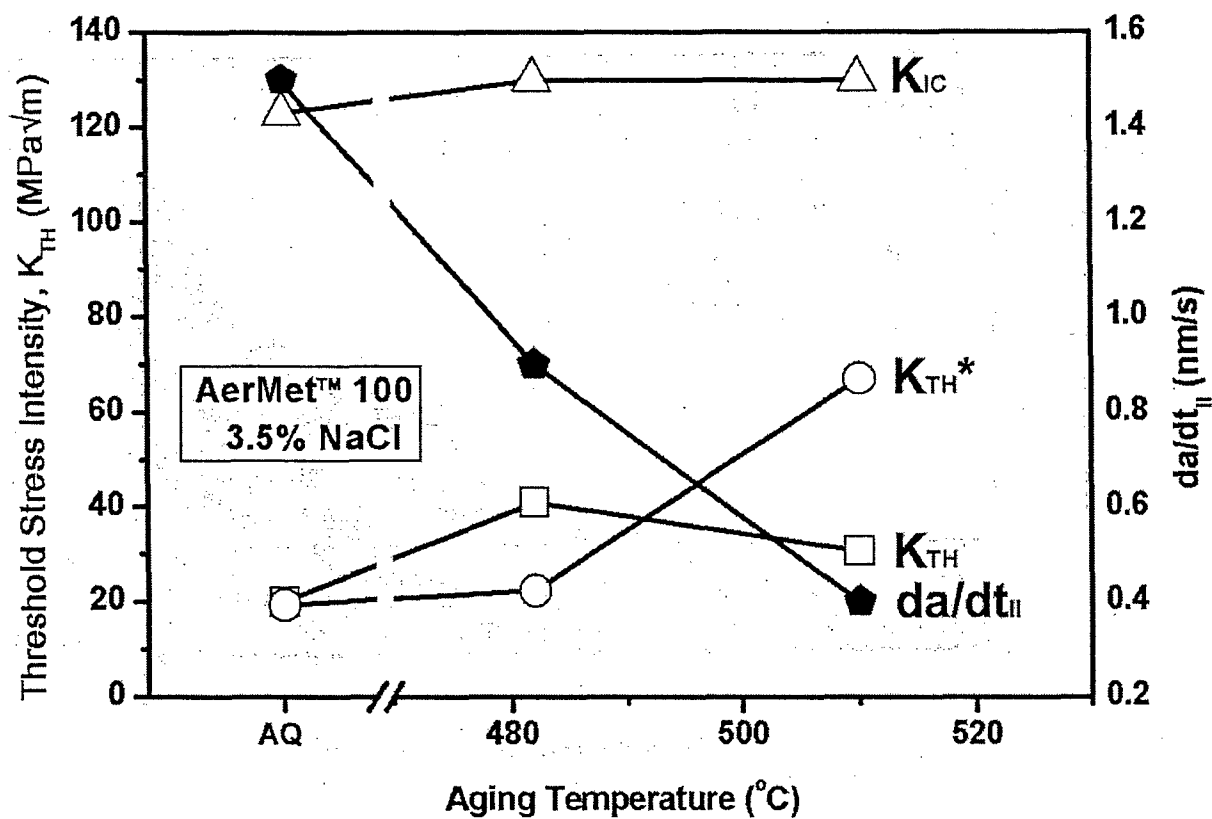


**Figure 5** Threshold stress intensity,  $K_{TH}$ , and  $da/dt_{II}$  vs. applied potential for various ages of AerMet™100 stressed in 3.5 % NaCl at applied potential of  $-0.625 V_{SCE}$ . The  $K_{IC}$  for each tempering condition is displayed for reference.

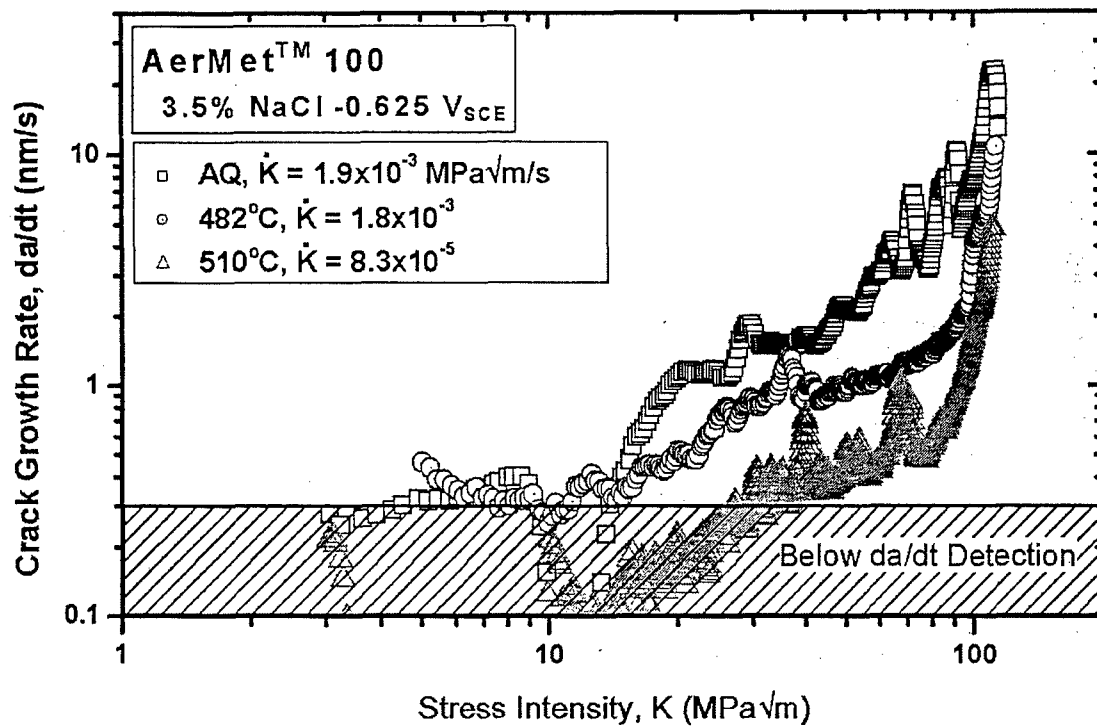


**Figure 6** Subcritical crack growth rate vs.  $K$ , for various aging temperatures of AerMet™ 100 stressed in 3.5 % NaCl at  $E_{\text{App}}$  of -0.625 V<sub>SCE</sub>. The initial loading rate,  $dK/dt$ , is noted.

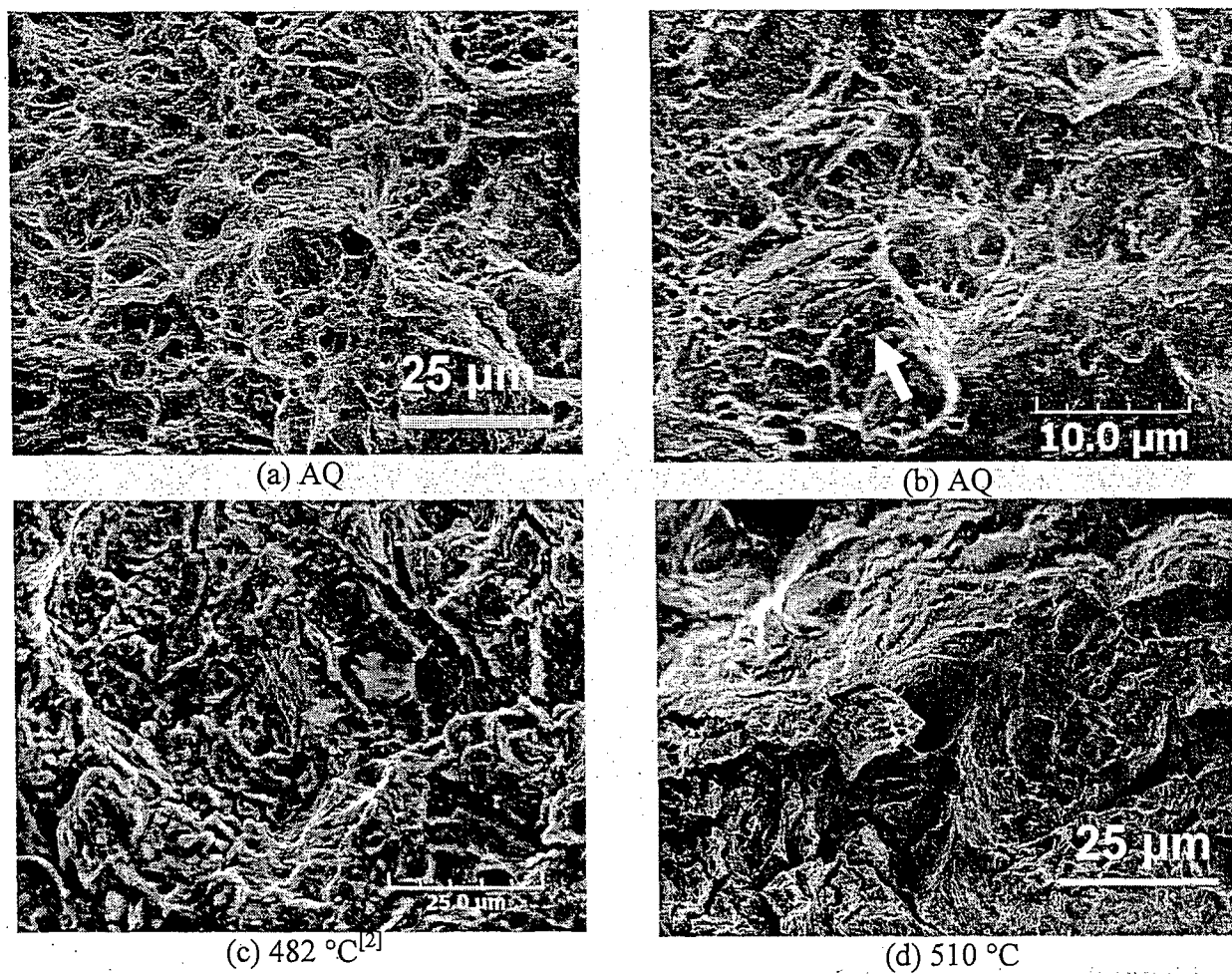


**Figure 7** SEM images of HEAC surfaces for various aging conditions of AerMet™ 100 stressed in 3.5 % NaCl at an applied potential of  $-0.625 \text{ V}_{\text{SCE}}$ . All images show predominantly transgranular fracture.

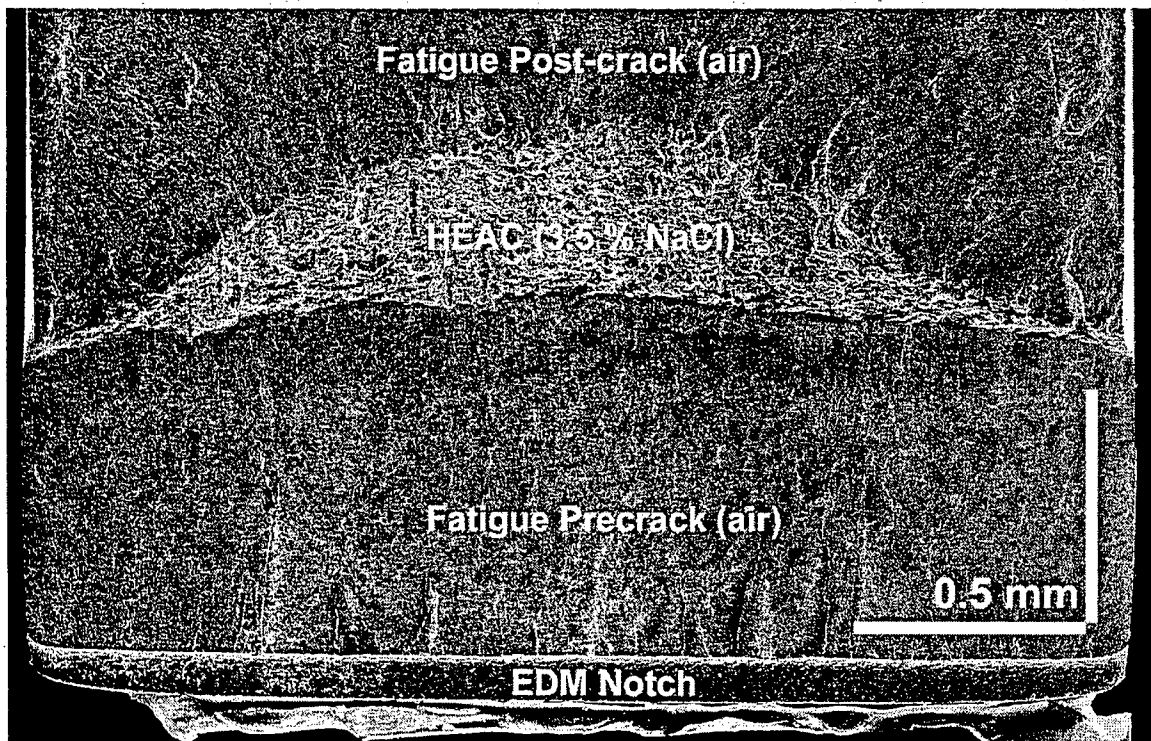


**Figure 8** Low magnification scanning electron fractograph of the fracture surface of an as-quenched (AQ) AerMet™ 100 specimen cracked in 3.5% NaCl polarized to  $-0.625 V_{SCE}$ . The thumbnail region marked "HEAC" represents subcritical HEAC extending over an average of  $240 \mu\text{m}$  for the loading range from  $K$  of 5 to  $80 \text{ MPa}\sqrt{\text{m}}$ . The post-test fatigue crack clearly marks the extent of HEAC.

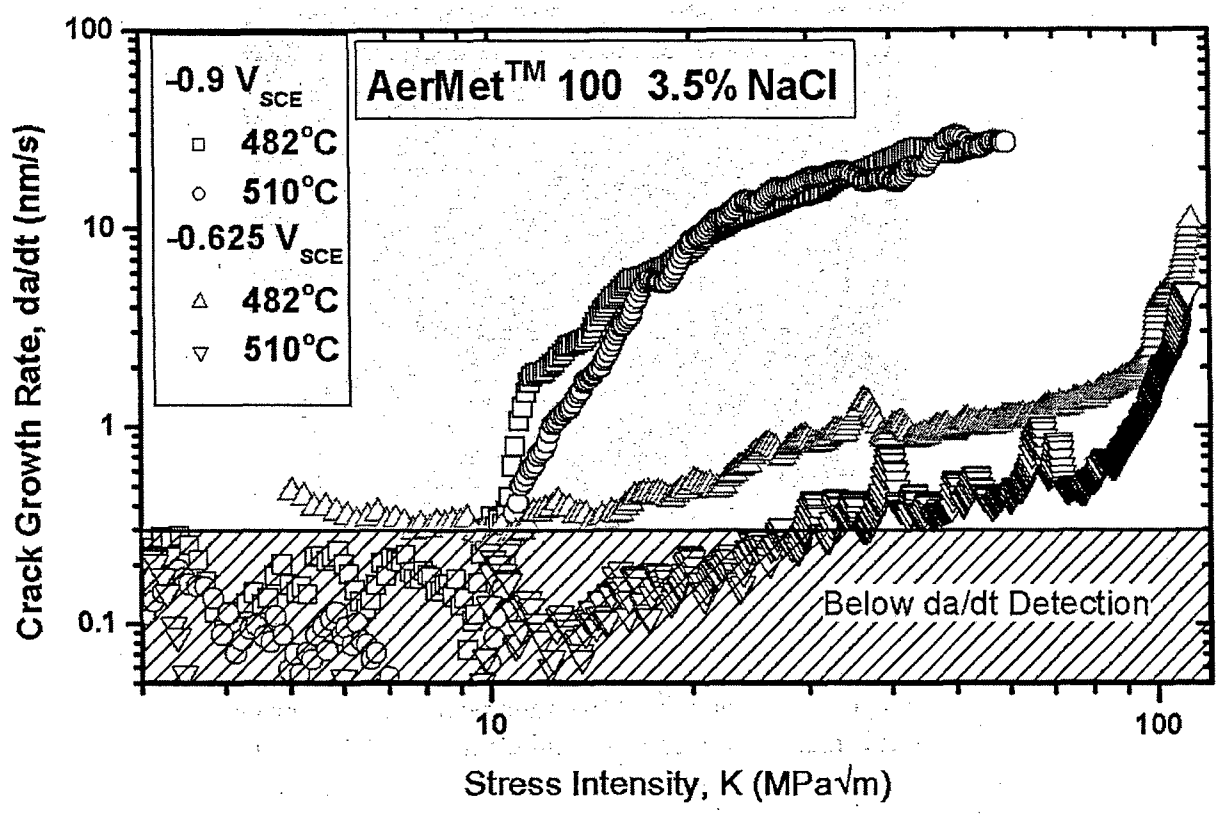
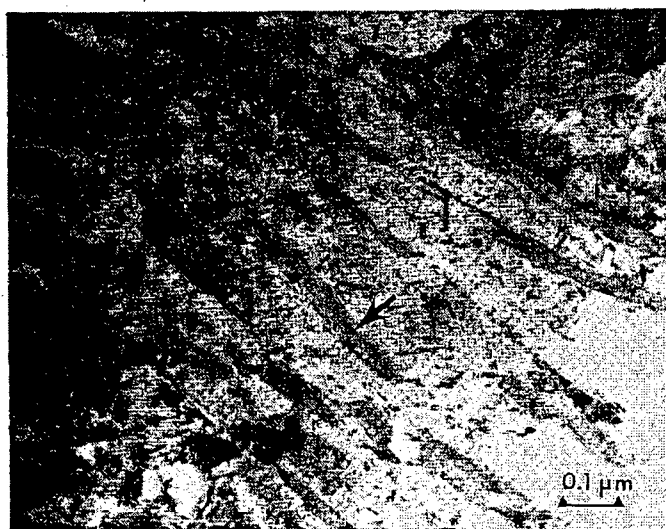


Figure 9 Subcritical crack growth rate vs.  $K$  for two aging temperatures of AerMet™ 100 stressed in 3.5 % NaCl. These two aging temperatures produce the highest toughness and strength in this steel.



**Figure 10** Transmission electron microscope image of AerMet™ 100 tempered at 538°C; bright field image of reversed austenite (arrow). Image and caption taken from Ayer and Machmeier<sup>[6]</sup>

## References

1. Richard L.S. Thomas, John R. Scully and Richard P. Gangloff: *Metallurgical Transactions A*, 2003, vol. 34A, pp. 327-44.
2. Yongwon Lee and R. P. Gangloff: University of Virginia, unpublished research, 2005.
3. Richard P. Gangloff: *Environmentally Assisted Failure*, Elsevier Ltd., 2003, pp. 31-101.
4. Richard L.S. Thomas, Daoming Li, Richard P. Gangloff and John Scully: *Metallurgical Transactions A*, 2002, vol. 33A, pp. 1991-2004.
5. Daoming Li, Richard P. Gangloff and John R. Scully: *Metallurgical and Materials Transactions A*, 2004, vol. 35A, pp. 849-64.
6. R. Ayer and P.M. Machmeier: *Metallurgical Transactions A*, 1993, vol. 24A, pp. 1943-55.
7. R. Ayer and P. M. Machmeier: *Metallurgical and Materials Transactions A*, 1998, vol. 29A, pp. 903-05.
8. Hyuck Mo Lee, Hyunchul Sohn and Choong Hwa Yoo: *Scripta Materialia*, 1997, vol. 37, pp. 1931-37.
9. Choong Hwa Yoo, Hyuck Mo Lee, Jin W. Chan and J. W. Morris Jr.: *Metallurgical and Materials Transactions A*, 1996, vol. 27A, pp. 3466-72.
10. P. M. Novotny: *Gilbert R. Speich Symposium-Fundamentals of Aging and Tempering in Bainitic and Martensitic Steel Products*, Iron and Steel Society, Warrendale, PA, 1992, pp. 215-36.
11. B.G. Pound: *Hydrogen Effects on Material Behavior and Corrosion Deformation Interactions*, The Minerals, Metals & Materials Society, Warrendale, PA, 2003, pp. 93-103.
12. B.G. Pound: *Acta Metallurgica*, 1998, vol. 46, pp. 5733-43.
13. E. U. Lee, H. Sanders and B. Sarkar: *Tri-Service Conference on Corrosion*, US Army Research Laboratory, 1999.
14. P.F. Buckley, R. Brown, G.H. Graces, E.U. Lee, C.E. Neu and J. Kozol: *Metallic Materials for Lightweight Applications-Proceedings of the 40<sup>th</sup> Sagamore Army Materials Research Conference*, United States Army Laboratory Command, Watertown, MA, 1993.
15. J. Kozol and C. E. Neu: Report No. NAWCADWAR-92018-60, Naval Air Warfare Center, Warminster, PA, Jan 10, 1992.
16. H.H. Johnson: *Materials Research & Standards*, 1965, vol. 5, pp. 442-45.

17. R.P. Gangloff, D.C. Slavik, R.S. Piascik and R.H. Van Stone: *Small Crack Test Methods*, ASTM STP 1149, J.M. Larsen and J.E. Allison, eds., ASTM International, West Conshohocken, PA, 1992, pp. 116-168.
18. M.J. Haynes and R.P. Gangloff: *Journal of Testing and Evaluation*, 1997, vol. 25, pp. 82-98.
19. E. U. Lee: *Metallurgical and Materials Transactions A*, 1995, vol. 26A, pp. 1313-16.
20. C.J. McMahon Jr.: *Engineering Fracture Mechanics*, 2001, vol. 68, pp. 773-88.
21. R. P. Gangloff: *Hydrogen Effects on Material Behavior and Corrosion Deformation Interactions*, The Minerals, Metals & Materials Society, Warrendale, PA, 2003, pp. 477-97.
22. R. W. J. Koers, A. H. M. Krom and A. Bakker: *Environmentally Assisted Cracking: Predictive Methods for Risk Assessment and Evaluation of Materials, Equipment, and Structures*, ASTM International, West Conshohocken, PA, 2000, pp. 303-16.
23. R. P. Gangloff: *Metallurgical Transactions A*, 1985, vol. 16A, pp. 953-69.
24. R.P. Gangloff and A. Turnbull: *Modeling Environmental Effects on Crack Initiation and Propagation*, The Minerals, Metals & Materials Society, Warrendale, PA, 1986, pp. 55-81.
25. E. U. Lee: Report No. NAWCADWAR-94001-60, Naval Air Warfare Center, Warminster, PA, Oct. 23, 1993.
26. C.L. Briant and S.K. Banerji: *Treatise on Materials Science and Technology, Embrittlement of Engineering Alloys*, Vol. 25, Academic Press, New York, NY, 1983, pp. 21-58.
27. Y. H. Kim, H. J. Kim and J. W. Morris Jr.: *Metallurgical and Materials Transactions A*, 1986, vol. 17A, pp. 1157-64.
28. M. L. Holzworth and M. R. Louthan Jr.: *Corrosion*, 1968, vol. 24, pp. 110-24.